Nano Research

Open Access

Research Article

Bionic coral reef inspired enhanced scattering of trimetallic LDH self assembled $Ti_3C_2T_x$ MXene for advanced microwave absorption

Yuntong Meng[1], Bo Cai[2], Yongtao Zhou[3], Lu Zhou[2], Yu Zhang[2], Jiahui Wang[1], Gegen Sarula[1], Luting Yan[1] ✉, Min Lu[4] ✉, Benliang Liang[1] ✉, and Guangsheng Wang[2]

[1] *School of Physical Science and Engineering, Beijing Jiaotong University, Beijing 100044, China*
[2] *Key Laboratory of Bio-Inspired Smart Interfacial Science and Technology of Ministry of Education, School of Chemistry, Beihang University, Beijing 100191, China*
[3] *PipeChina Beijing Pipeline Company, Ltd., Beijing 100101, China*
[4] *School of Chemical Engineering, Northeast Electric Power University, Jilin 132000, China*

Cite this article: *Nano Research*, **2025**, *18*, 94907842. https://doi.org/10.26599/NR.2025.94907842

ABSTRACT: Electromagnetic wave radiation disrupts electronic devices and threatens human health. Microwave absorbing materials are essential for addressing electromagnetic pollution and military stealth applications. Advancement of electronics creates demand for absorbers with thin thickness, light weight, wide bandwidth, and strong absorption. Conventional materials suffer from poor impedance matching and limited loss mechanisms in the Ku band. Heterojunction engineering offers solutions through control of band alignment and charge distribution. The built-in electric field serves as a core mechanism for enhancing dielectric loss. However, limitations exist in understanding of formation mechanisms of built-in electric fields in multi-interface systems. This study develops a ZnNiCo-LDH/MXene composite with coral-inspired architecture. Construction of high-density Mott–Schottky interfaces occurs through electrostatic assembly of polar semiconductor units and conductive matrices. Vertical growth of flower-like layered double hydroxide (LDH) on MXene extends propagation paths of electromagnetic waves. This design creates continuous networks of built-in electric fields. Enhanced charge separation and interfacial polarization result. Performance demonstrates −49.6 dB reflection loss at 1.35 mm thickness. Effective bandwidth reaches 3.4 GHz across Ku-band frequencies. Radar cross-section simulations confirm −39.57 dB·m² signal suppression. These achievements meet requirements of advanced absorbers. The work establishes a new paradigm for manipulation of built-in electric fields through multi-interface engineering.

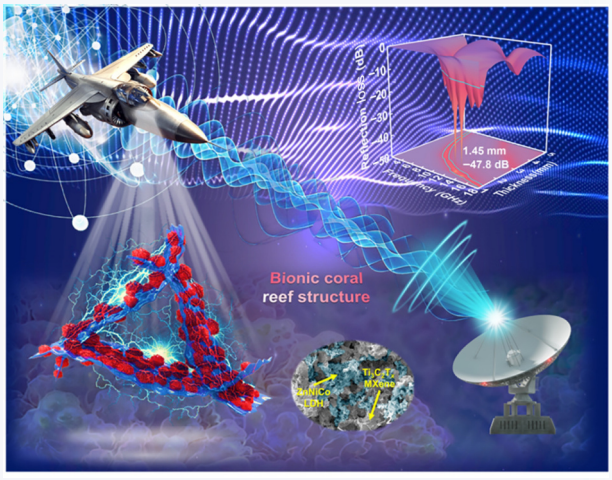

KEYWORDS: built-in electric field, ZnNiCo LDH@$Ti_3C_2T_x$ MXene, heterojunction engineering, bioinspired coral-like

1 Introduction

Electromagnetic wave (EMW) radiation not only interferes with the normal operation of electronic devices but also poses a potential threat to human health [1–3]. Microwave absorbing materials (MAMs) are crucial for addressing modern electromagnetic pollution and enhancing military stealth technology. They play an indispensable role in 5G communication, electronic device shielding, and defense security [4–6]. As electronics advance toward higher frequencies and greater integration, there is an urgent need for new generation MAMs that are thin, lightweight, wide-band, and strong-absorption [7–11]. Conventional MAMs face challenges such as poor impedance matching, limited loss mechanisms, complex preparation processes, and insufficient performance stability, especially in the high frequency Ku band. These issues arise from the contradiction between material properties and

Received: June 26, 2025; **Revised:** July 22, 2025
Accepted: July 24, 2025

✉Address correspondence to Luting Yan, ltyan@bjtu.edu.cn; Min Lu, lumin19770919@163.com; Benliang Liang, blliang@bjtu.edu.cn

structural design. High conductivity benefits Ohmic loss but impairs impedance matching. Excessive reliance on dielectric loss can lead to narrow absorption bands and increased thickness [12, 13]. To overcome these limitations, novel material design paradigms are needed. Focus should be placed on regulating electronic behavior and interfacial energy conversion. Heterojunction engineering has emerged as a key strategy for tailoring electromagnetic responses [14, 15]. By constructing semiconductor conductor heterojunctions, this approach enables precise control of electronic band alignment, spatial charge distribution, and electron transport pathways. This allows for directional optimization of MAM absorption performance. For example, Gu et al. [16] prepared heterostructured BN@Co-C@C/polyethylene terephthalate (PET) composites via one-pot synthesis of BN@ZIF-67@PDA precursor followed by pyrolysis, which exhibited excellent thermal conductivity (5.37 $W \cdot m^{-1} \cdot K^{-1}$, 35.8 times that of pure PET) and microwave absorption performance at C band (minimum reflection loss of −63.1 dB at 4.72 GHz with an effective absorption bandwidth of 1.28 GHz) when the mass ratio of BN to ZIF-67@PDA was 7.5:1 and the filler content was 45 wt.%. Zhan et al. [17] developed multifunctional cellular carbon foams from chitosan via freeze-drying and carbonization, which exhibit efficient microwave absorption, self-cleaning, and thermal insulation properties, providing a strategy for developing high-performance multifunctional microwave absorbers. He et al. [18] fabricated shape anisotropic chain-like CoNi/polydimethylsiloxane composite films, which exhibit excellent low-frequency microwave absorption (minimum reflection loss of −56.7 dB and effective absorption bandwidth of 1.04 GHz at 18 vol.%) and high thermal conductivity (in-plane 2.05 $W \cdot m^{-1} \cdot K^{-1}$ and inter-plane 0.61 $W \cdot m^{-1} \cdot K^{-1}$), providing new insights for applications in 5G communications and flexible electronics.

Among various interfacial effects, the built-in electric field (BIEF) is particularly significant. BIEF is a static electric field driven by Fermi level equilibrium. It can effectively promote charge separation, enhance interfacial polarization losses, and improve electromagnetic energy conversion efficiency [19]. BIEF is most prominent in P–N junctions and Mott–Schottky interfaces, making it a core mechanism for boosting dielectric loss [20, 21]. For example, Zhan et al. [22] engineered two-dimensional/three-dimensional (2D/3D) van der Waals heterostructures of reduced graphene oxide/carbon foams (RGO/CFs) via a mixed-dimensional assembly strategy (freeze-drying, immersion absorption, secondary freeze-drying, and carbonization), which exhibit excellent microwave absorption, corrosion resistance, and thermal insulation, with tunable electromagnetic properties by regulating RGO content and carbonization temperature. However, current research on BIEF based heterojunction engineering has clear limitations [23]. Most studies focus on single type heterojunctions. The formation mechanisms and quantitative control of BIEF remain unclear, especially regarding charge transfer, band bending, and polarization loss at microscopic scales [24]. For example, this lack of understanding hinders the rational design of high performance MAMs [25, 26].

To solve these challenges, this study presents a bio-inspired coral reef like hierarchical structure. Heterojunction engineering has led to the development of the ZnNiCo LDH@$Ti_3C_2T_x$ MXene composite (ZNCM). A breakthrough in enhancing the electromagnetic characteristics of materials has been achieved. Polar semiconductor units, composed of Zn, Ni, and Co based layered double hydroxide (LDH), are utilized in the design. Optimization of the electronic structure and the incorporation of flower-like nanostructures are featured in these units. Numerous polarization sites and scattering interfaces are offered by such structures. The conductive MXene matrix, with its high carrier concentration and surface functional groups like –O, –OH, and –F, forms an electron transport network. Through electrostatic interaction between oppositely charged species, the two components assemble themselves. A tight 2D/2D interface is created, and high density Schottky barriers are induced. Mimicking the multi-level open porous structure of coral reefs, the LDH nanoflowers grown vertically on the MXene matrix form a "coral-polyp" bio inspired configuration. This increases the interfacial binding strength and charge transfer efficiency while extending the propagation paths of electromagnetic waves through multiple reflections.

The synthesized ZNCM heterostructure demonstrates exceptional performance. It achieves −49.6 dB reflection loss at 1.35 mm thickness, equivalent to 99.998% electromagnetic energy absorption. It also has a 3.4 GHz effective bandwidth covering the Ku-band radar frequencies (12–18 GHz). Radar cross section (RCS) simulations validate −39.57 $dB \cdot m^2$ signal suppression, proving its potential in next generation stealth platforms. These results meet the "thin, light, wide, strong" requirements of advanced absorbers. Thus, this work offers a new bio inspired strategy for designing and manufacturing advanced electromagnetic wave absorption materials, providing a way to overcome existing performance barriers.

2 Experimental

2.1 Synthesis of MXene nanoplates

An aqueous HCl solution (9 M, 20 mL) was used to disperse 1.6 g of lithium fluoride (LiF). Over a 10-minute period, 1.0 g of Ti_3AlC_2 was gradually introduced into this mixture. Following 24 h of continuous stirring and etching at 35 °C, the resulting solution underwent repeated washing with deionized water and multiple centrifugation cycles at 3500 rpm until a pH of 6 was achieved. Next, the precipitate underwent 60 min of ultrasonic treatment under argon flow, followed by 30 min of centrifugation at 3500 rpm. Ultimately, the dark green $Ti_3C_2T_x$ supernatant was harvested for further analysis.

2.2 Synthesis of ZnCo ZIF and ZnNiCo LDH

ZnCo ZIF was synthesized through a template-mediated approach beginning with the preparation of ZnO nanosheets. $Zn(Ac)_2 \cdot 2H_2O$ (15 mmol) and HMTA (25 mmol) were dissolved in deionized water (60 mL), followed by rapid addition of NaOH (1 g) under vigorous stirring for 2 h. The resulting product was washed with water/ethanol and vacuum-dried (60 °C, 24 h). Subsequently, these ZnO nanosheets (0.5 g) were dispersed in H_2O (24 mL) and combined with a DMF solution (72 mL) containing 2-methylimidazole (4 g), then reacted at 70 °C for 10 h to yield ZnO@ZIF-8 after washing and drying. For ZnCo ZIF formation, ZnO@ZIF-8 (0.5 g) was dispersed in methanol (30 mL) via sonication (30 min), followed by sequential addition of $Co(NO_3)_2$ (0.9 g) and 2-MI (3.28 g) in methanol (100 mL). The mixture was stirred at room temperature for 24 h. Finally, ZIF-8/67 (80 mg) was dissolved in ethanol (100 mL) with $Co(NO_3)_2 \cdot 6H_2O$ (200 mg),

$Ni(NO_3)_2{\cdot}6H_2O$ (200 mg), and HMTA (120 mg). The solution was refluxed at 80 °C for 1 h, then centrifuged, washed with ethanol, and vacuum-dried to obtain light green ZnNiCo LDH powder.

2.3 Preparation of ZNCM

The hierarchical ZNCM nanocomposite was fabricated through an electrostatic self-assembly method. Initially, 0.03 g of ZnNiCo LDH was evenly dispersed in 20 mL of deionized water. Subsequently, a $Ti_3C_2T_x$ nanosheet suspension (1.0 mg·mL^{-1}) was incorporated. After being stirred for 20 min, the ZNCM composite material was formed and collected via freeze-drying. The resulting composite is referred to as ZNCM-*x*, with *x* (10, 20, 30) corresponding to the volume of the $Ti_3C_2T_x$ MXene suspension. The specific sample usage is provided in Table S1 in the Electronic Supplementary Material (ESM).

2.4 Characterization

The crystal structure of the synthesized product was analyzed using X-ray diffraction (XRD), carried out on a Bruker D8 AVANCE diffractometer equipped with Cu Kα radiation. The morphology and nanostructure were examined through field emission scanning electron microscopy (SEM, JSM-7500F) and transmission electron microscopy (TEM, JEM-2100F). The surface chemical composition was investigated via X-ray photoelectron spectroscopy (XPS) using a Thermo Escalab 250Xi spectrometer. The zeta potential measurements were performed with a Malvern Zetasizer Nano ZS (Malvern Instruments, USA). To assess the electromagnetic parameters, the product was blended with varying mass percentages of PVDF and formed into circular ring shapes (outer diameter Φ_{out} = 7.00 mm, inner diameter Φ_{in} = 3.04 mm). The electromagnetic properties were then determined using a vector network analyzer (VNA; Agilent TE5071C). The specific amounts of PVDF and the sample used for different filling ratios are detailed in Table S2 in the ESM.

2.5 RCS Simulations

The electromagnetic simulation was performed using CST STUDIO SUITE 2014. The entire simulation process was carried out under open boundary conditions and linearly polarized planar electromagnetic waves were added. A model was constructed in the *XY*-plane, consisting of a 200 mm × 200 mm × 2 mm absorbing coating evenly applied over a perfect electric conductor plate measuring 200 mm × 200 mm × 1 mm. The model was exposed to an incident EMW originating from the negative *Z*-axis, with the magnetic field aligned parallel and the electric field perpendicular to the *X*-axis. The RCS values were recorded for incidence angles spanning from 0° to 180°, and the calculations were based on Eq. (1) [20]

$$\sigma\,(\mathrm{dB{\cdot}m^2}) = 10\lg\left(\frac{4\pi S}{\lambda^2}\left|\frac{E_s}{E_i}\right|\right)^2 \quad (1)$$

In the formula, *S* indicates the area of the model, λ stands for the wavelength of the incident wave, and E_s and E_i represent the electric field intensities of the scattered and incident waves, respectively.

3 Results and discussion

Preparation process and structure of hierarchical ZNCM are illustrated in Fig. 1. Its three-dimensional hierarchical architecture is constructed using a zinc oxide-derived bimetallic ZIF precursor as a template. Opposite electronegativity between LDH and MXene nanosheets facilitates electrostatic self-assembly. Initially, zinc oxide is dissolved by imidazole to release zinc ions, which are subsequently assembled with cobalt ions to form ZIF-8/67. Subsequently, ZnCo ZIF is etched by nickel nitrate and HMTA, triggering the release of Zn^{2+} and Co^{2+} ions from the framework. Concurrently, Co^{2+} is partially oxidized to Co^{3+} by NO_3^- and dissolved oxygen. Eventually, the co-precipitation of Co^{2+}/Co^{3+} and Ni^{2+} drives the formation of ZnCoNi LDH nanoflowers. Owing to

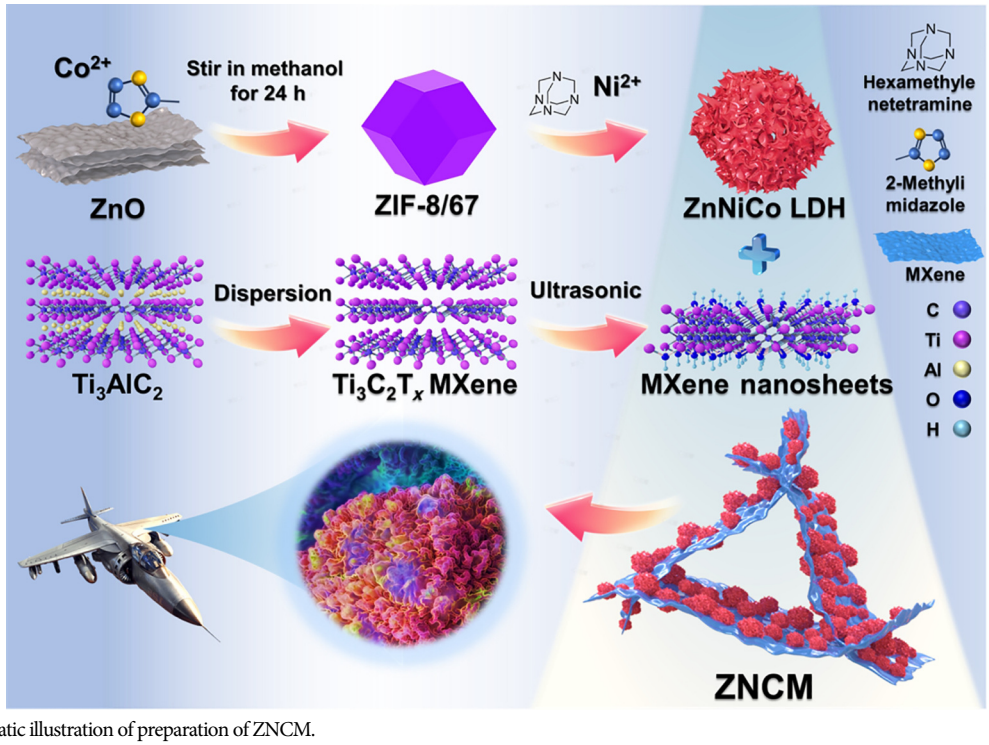

Figure 1 The schematic illustration of preparation of ZNCM.

their opposite electronegativity, LDH and MXene nanosheets undergo electrostatic self-assembly in an aqueous solution to construct a three-dimensional architecture. During electrostatic self-assembly, the high electronegativity of MXene primarily induces the exfoliation of the outer layers of LDH nanoflowers into nanosheets, while the inner framework remains intact. This partial decomposition does not destroy the three-dimensional porous architecture but rather generates more exposed interfaces and interconnected channels. As a result, the modified structure still maintains the porous and rough surface characteristics required for multiple scattering of electromagnetic waves, while the newly formed 2D/2D interfaces between LDH nanosheets and MXene enhance interfacial polarization. In this system, the composition ratio of the three-dimensional framework has a close relationship with the loss and attenuation of electromagnetic waves. Additionally, the fine electrical conductivity of MXene can significantly enhance the electromagnetic wave absorption performance of the composite material. Conductive network-induced conduction loss and interfacial polarization act synergistically. These effects enable the EMW absorber to achieve lower RL, wider EAB, and thinner thickness, meeting the "thin, light-weight, wide-band, strong-absorption" design criteria. Higher interfacial barriers and increased energy band bending can enhance charge separation, thereby boosting interfacial polarization.

XRD was used to characterize the composition and structural features of the resulting samples. Selectively etching the Al layer of pristine Ti_3AlC_2 successfully realized the exfoliation of $Ti_3C_2T_x$ MXene nanosheets. As shown in Fig. 2(a), the disappearance of the most intense diffraction peak around 39° in the $Ti_3C_2T_x$ MXene map indicates that the Al layer was selectively removed. XRD

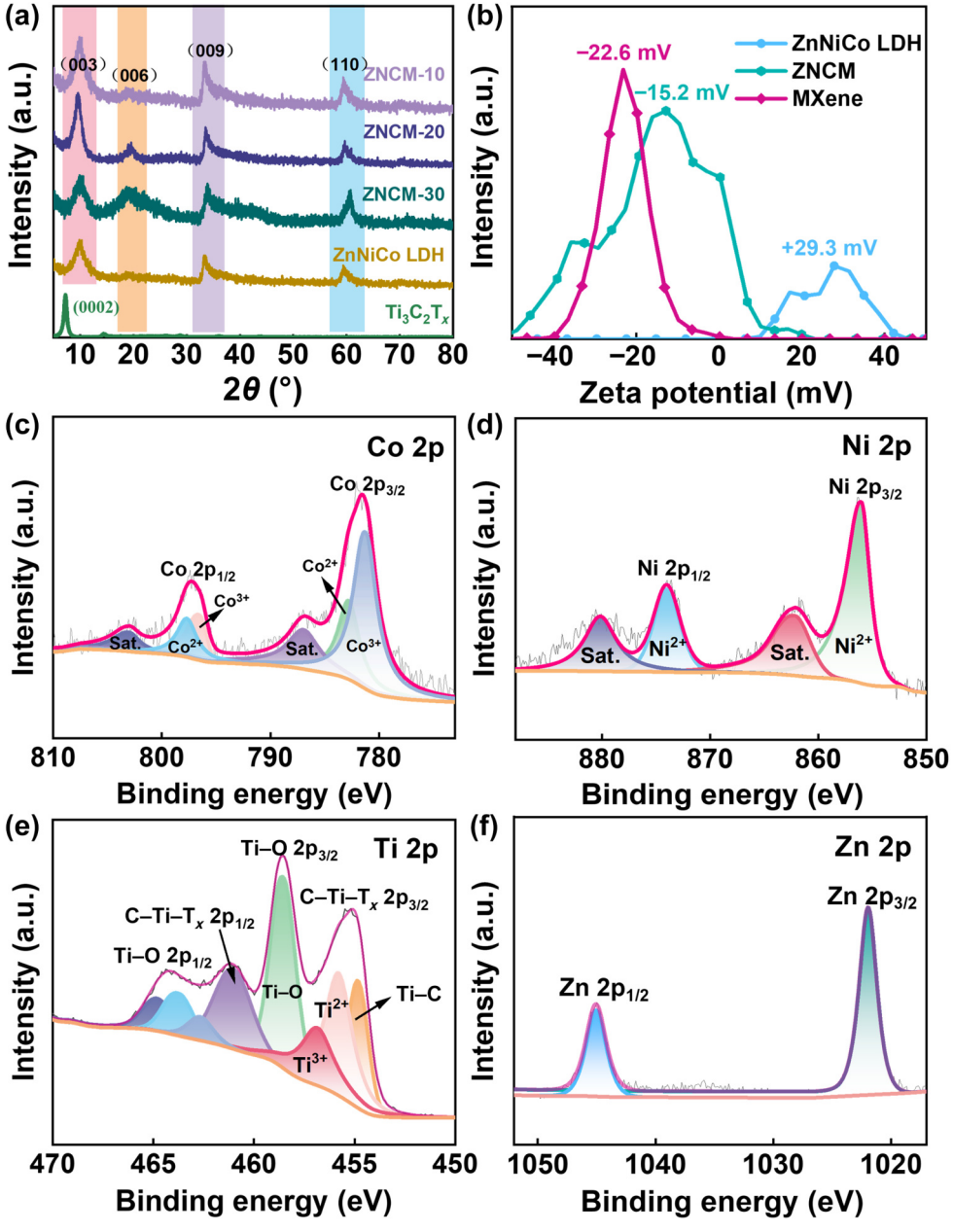

Figure 2 (a) XRD plots of ZnNiCo LDH, $Ti_3C_2T_x$, ZNCM-10, ZNCM-20, and ZNCM-30. (b) Zeta potential plots of ZnNiCo LDH, ZNCM, and MXene. (c) Co 2p, (d) Ni 2p, (e) Ti 2p, and (f) Zn 2p spectra of ZNCM-10.

analysis reveals six peaks at 7.06°, 14.33°, 21.21°, 28.75°, 36.12°, and 43.90° for $Ti_3C_2T_x$ nanosheets, corresponding to the (002), (004), (006), (008), (0010), and (0012) crystal planes [12]. The XRD spectrum of ZIF 8/67 (Fig. S1 in the ESM) is in good agreement with the ZIF standard card [27]. The main diffraction peaks for the ZnNiCo LDH sample appear at 10.37°, 23.13°, 33.67°, and 59.90°, corresponding to the (003), (006), (009), and (110) facets of typical LDH [28]. After electrostatic self-assembly, the new peaks around 5° represent the ZnNiCo LDH was successfully combined with $Ti_3C_2T_x$ MXene nanosheets [29]. A further increase in layer spacing suggests that the three-dimensional structure of ZnNiCo LDH effectively mitigates MXene nanosheet self-stacking, enriching interfaces and lengthening electromagnetic wave propagation paths. As shown in Fig. 2(b), due to the rich surface functional groups (–O, –OH and –F) generated by the etching treatment, the $Ti_3C_2T_x$ nanosheets are negatively charged with a ζ potential of −22.6 mV, enabling electrostatic interaction with positively charged ZnNiCo LDH (+ 29.3 mV).

XPS was also used to prove the covalent state and valence state information of elements. It is found that the ZNCM composite is mainly composed of Zn, Ni, Co, C, Ti and O elements (Fig. S2(a) in the ESM), confirming the combination of ZnNiCo LDH and $Ti_3C_2T_x$ MXene nanosheets [30, 31]. As can be seen from Fig. S2(b) in the ESM, the C 1s binding energies of the ZNCM composite are 281.65, 284.83, 286.24, and 288.67 eV, respectively, belonging to O–C=O, C–O, C–C and C–Ti [32]. Two spin dipole orbits (labeled Co $2p_{3/2}$ and Co $2p_{1/2}$) and two shakeup satellites are present in the deconvoluted Co 2p spectrum (Fig. 2(c)). Peaks at binding energies of 782.80 and 797.70 eV correspond to Co^{2+} $2p_{3/2}$ and $2p_{1/2}$, respectively, whereas those at 781.22 and 796.54 eV are assigned to Co^{3+} $2p_{3/2}$ and $2p_{1/2}$ [33, 34]. Ni has two peaks at 856.04 and 874.01 eV, corresponding to the orbital peaks of Ni^{2+} $2p_{3/2}$ and $2p_{1/2}$. Binding energy splitting of 17.7 eV characterizes Ni^{2+} (Fig. 2(d)). Figure 2(e) displays four peaks of the ZNCM composite at 454.83, 455.80, 456.85, and 458.53 eV correspond to Ti–C, Ti^{2+}, Ti^{3+}, and Ti–O, respectively. Splitting of the Zn 2p orbital into Zn^{2+} $2p_{3/2}$ and $2p_{1/2}$ occurs at 1021.94 and 1045.04 eV, indicating the presence of Zn^{2+} (Fig. 2(f)) [28]. XPS analysis reveals that the $Ti_3C_2T_x$ MXene and ZnNiCo-LDH combine successfully through strong covalent bond interaction [35].

Scanning electron microscopy (SEM) reveals that the lateral dimension of the obtained $Ti_3C_2T_x$ flakes is approximately 1 μm. Figures S3(a) and S3(b) in the ESM show the ZnCo ZIF precursor exhibits a rhombic dodecahedral structure with a smooth surface and relatively uniform dimensions in the range of 50–100 nm. Under the action of hexamethylenetetramine, ZnNiCo LDH is assembled into nanoflowers through interlaced nanosheets, presenting an overall shape similar to that of a coral reef (Figs. S3(c) and S3(d) in the ESM). Figures 3(a)–3(c) show the ZNCM with different contents of MXene. Due to the significant difference in the sizes of MXene and LDH, when the MXene content increases, the uniformity of the composite material decreases, and larger pores begin to emerge. Moreover, the magnified SEM images (Figs. 3(d)–3(f)) clearly demonstrate the highly porous interconnected architecture of the ZNCM skeleton. This unique microstructure promotes multiple reflections and effective attenuation of EMW, thereby significantly enhancing the EMW absorption performance. Elemental composition of ZNCM is displayed in Fig. S4 in the ESM. Notably, MXene nanosheets can serve as a structural network for adsorbing ZnNiCo LDH and also as a conductive network for conduction loss. Accelerated electron mobility promotes more efficient conversion of electromagnetic energy into thermal energy. Varying the LDH/MXene ratio systematically adjusts heterointerface density, achieving controlled interface modulation. TEM and HRTEM were used to further analyze the microstructure of the hierarchical network. Figure S5 in

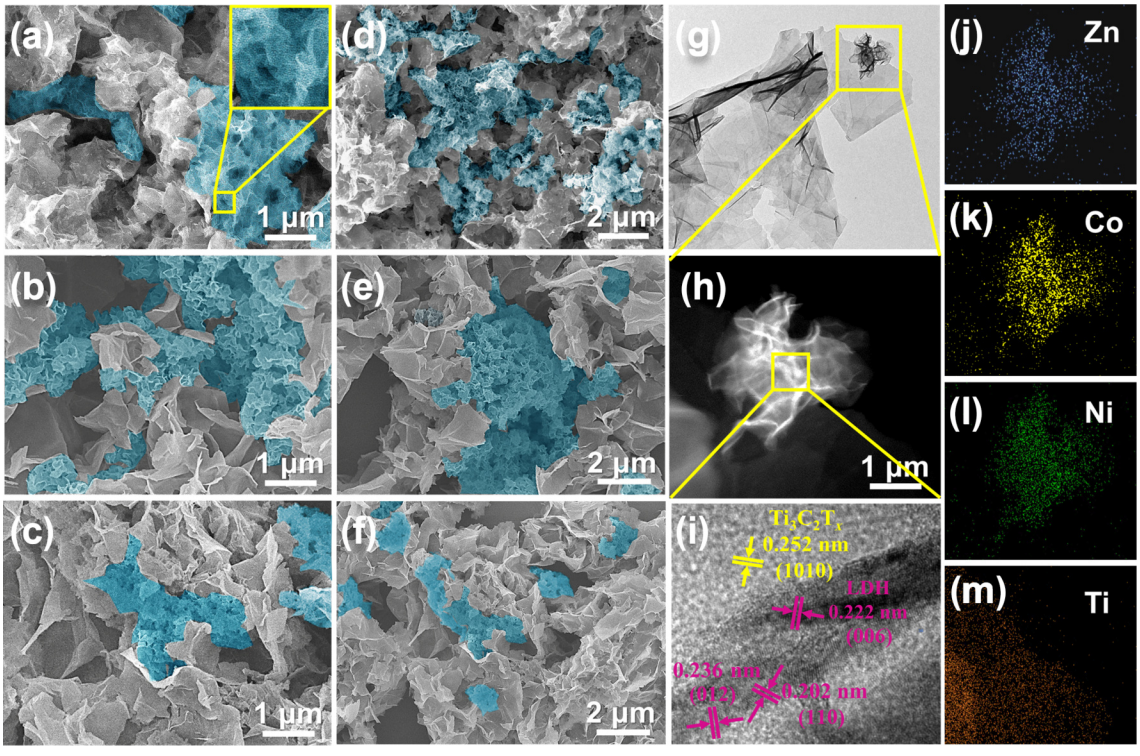

Figure 3 (a)–(c) SEM images and (d)–(f) low-magnification SEM images of ZNCM-10, ZNCM-20, and ZNCM-30. (g) and (h) TEM images of ZNCM-10. (i) HR-TEM image and (j)–(m) element mappings of ZNCM-10.

the ESM shows LDH nanoflowers are anchored on ultra-thin MXene nanosheets. By characterizing the lattice fringes of ZNCM by HRTEM (Figs. 3(g)–3(i)), it can be clearly seen that the lattice fringe of 0.252 nm belongs to the (0012) crystal plane of $Ti_3C_2T_x$ MXene [36, 37]. Lattice fringes of 0.202, 0.222, and 0.236 nm correspond to the (110), (006), and (012) crystal planes of LDH, respectively [12]. Additionally, element mapping analysis (Figs. 3(j)–3(m)) shows that Zn, Ni, Co, and Ti are evenly distributed, indicating that MXene has been successfully incorporated onto the LDH surface.

After a detailed study of the structural properties of the material, we turned our attention to the electromagnetic properties of the material. Material structural characteristics correlate closely with electromagnetic properties. In the field of electromagnetism, the complex dielectric constant ($\varepsilon_r = \varepsilon' - j\varepsilon''$) and complex permeability ($\mu_r = \mu' - j\mu''$) of materials are the key parameters characterizing their behavior in electromagnetic fields [38]. Complex dielectric constant real part (ε') signifies energy storage capacity, while imaginary part (ε'') indicates dissipation ability [38]. Similarly, complex permeability real (μ') and imaginary (μ'') parts relate to magnetic energy storage and dissipation, respectively [39, 40]. Loss tangents $\tan\delta_\varepsilon$ and $\tan\delta_\mu$ evaluate material dissipation, with $\tan\delta_\varepsilon = \varepsilon''/\varepsilon'$ and $\tan\delta_\mu = \mu''/\mu'$ representing dielectric and magnetic loss degrees [41, 42].

To evaluate the electromagnetic wave absorption performance of ZNCM composites, the electromagnetic parameters of various samples with PVDF as the substrate were measured within the frequency range of 2–18 GHz (Table S3 in the ESM). Figures S7(a)–S7(c) in the ESM and Figs. 4(a)–4(c) show that both the real and imaginary parts of the dielectric constant of $Ti_3C_2T_x$ are significantly higher than those of other samples. Extremely high electrical conductivity of MXene explains this, as pure LDH exhibits real and imaginary parts close to 1 and 0, respectively. Coupling pure $Ti_3C_2T_x$ MXene with coral reef-like LDH nanocages yields the ZNCM composite material. With the increase of the MXene composite content, both the ε'' and ε' values increased significantly, and the curve presented multiple resonance peaks, indicating that there was rich polarization behavior within the material [43]. Due to the huge electrical conductivity and the difference between positive and negative charges, a large number of built-in electric fields are formed at the interface between ZnNiCo LDH and $Tii_3C_2T_x$ MXene [44]. Charge difference between negatively charged $Ti_3C_2T_x$ MXene and positively charged ZnNiCo LDH drives this electric field, leading to charge redistribution. Similar to the Mot–Schottky effect in semiconductor junctions, the resulting charge separation generates built-in electric field (BIEF), enhancing charge migration and interface polarization under electromagnetic waves, and improving the attenuation and absorption capacity of the composite (Fig. S6 in the ESM) [45]. For $\tan\delta_\varepsilon$ and $\tan\delta_\mu$, a similar trend to that of ε_r and μ_r was observed. ZNCM nanocomposites show larger $\tan\delta_\varepsilon$ values with the increase of MXene, while their $\tan\delta_\mu$ values do not increase significantly [46]. Charge difference between negatively charged $Ti_3C_2T_x$ MXene and positively charged ZnNiCo LDH drives this electric field, leading to charge redistribution (Figs. S7(d)–S7(f) in the ESM) [47].

Attenuation constant (α) represents another key factor in determining the EM absorption performance. In order to gain a clearer understanding of the microwave absorption enhancement mechanism of the ZNCM composite, Fig. 4(d) presents the α [48, 49]: LDH sample exhibits the lowest α value, indicating its weakest microwave attenuation ability. ZNCM composites show a significant increase in α value after compounding with $Ti_3C_2T_x$ MXene, with slight fluctuations as MXene loading increases [50]. Visually, the influence of different packing loads on attenuation capacity is also observable. An increase in ZNCM loading from 20 wt.% to 30 wt.% leads to a significant improvement in the α value. Such improvement indicates excellent dielectric loss capacity of the material, which also aligns with the electromagnetic parameter results [51].

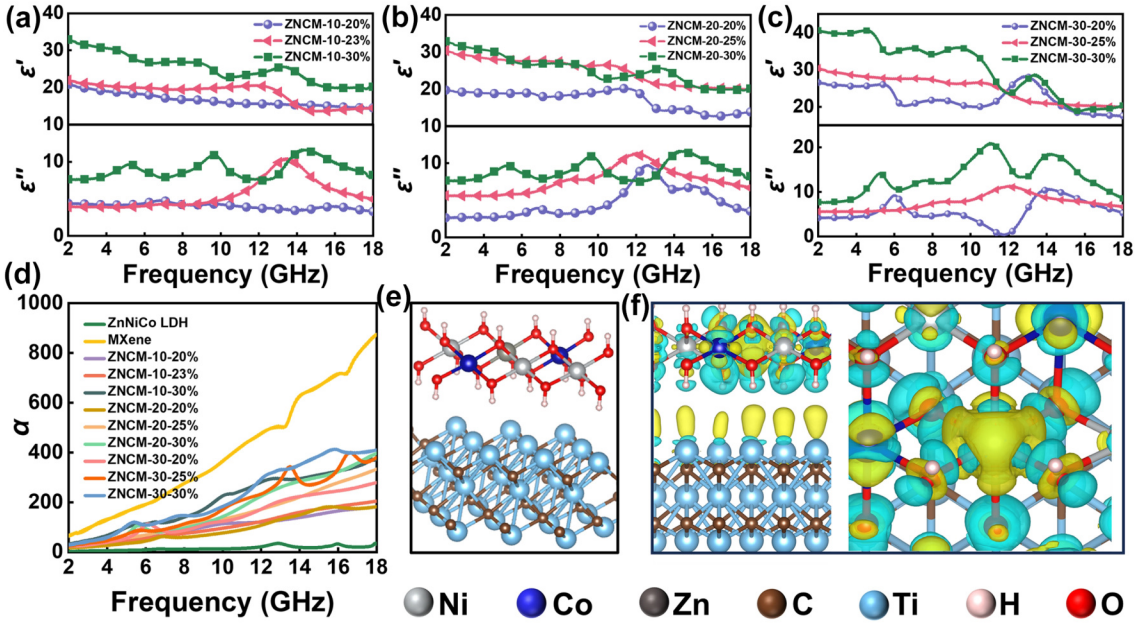

Figure 4 (a)–(c) The real and imaginary parts of the dielectric constant of ZNCM-10, ZNCM-20, and ZNCM-30 with different filling amounts in the range of 2–18 GHz. (d) Comparison chart of attenuation constants. (e) Schematic diagram of the ZNCM model and differential charge density diagram. (f) Schematic diagram of the electron cloud distribution of ZNCM.

$$\alpha = \frac{\sqrt{2}\pi f}{c}\sqrt{(\mu'\varepsilon'' - \mu'\varepsilon') + \sqrt{(\mu'\varepsilon'' - \mu'\varepsilon')^2 + (\mu''\varepsilon' - \mu'\varepsilon')^2}} \quad (2)$$

Dielectric loss is closely tied to conduction loss, multiple scattering, and polarization relaxation. These factors are often attributed to interfacial and dipole polarization [52]. In general, the Debye dipole relaxation process is a common way to explain the mechanism behind dielectric loss. Based on the Debye relaxation theory, the relationship between ε' and ε'' can be formulated as Eq. (3) [53]

$$\left(\varepsilon' - \frac{\varepsilon_s + \varepsilon_\infty}{2}\right)^2 + (\varepsilon'')^2 = \left(\frac{\varepsilon_s + \varepsilon_\infty}{2}\right)^2 \quad (3)$$

Here, ε_s and ε_∞ respectively represent the static dielectric constant and the relative dielectric constant at infinite frequencies. The results show that the ε' and ε'' curves can form a Cole–Cole curve, and each curve reflects a Debye relaxation process [54, 55]. There are multiple distorted semicircles on LDH, indicating that it is dominated by multiple scattering caused by a large number of interfaces (Figs. S8(a) and S8(b) in the ESM). Multiple distorted Cole–Cole curves were observed in the ZNCM composite material (Figs. S8(c)–S8(e) in the ESM), verifying the multipolarization relaxation behavior and the relaxation process occurring on the mesomagnetic parameters (Figs. S8(f)–S8(j) in the ESM). These relaxation processes include dipole polarization of the $Ti_3C_2T_x$ surface groups, bonding charges, and interfacial polarization caused by a large number of heterogeneous interface structures [56]. The ZNCM composite material has a stronger surface electromagnetic wave capture ability, dielectric loss, and more importantly, polarization loss of BIEF provided by a large number of heterogeneous interfaces.

Theoretical simulation analyzed the system interface effect of space charge engineering manipulation. Deep analysis of ZNCM nanocomposites spatial charge behavior was performed via differential charge density calculation. Differential charge density is evaluated through density functional theory (DFT) calculations. Due to the differences in the energy band structure, electrons and holes spontaneously diffuse at the heterogeneous interface, causing them to redistribute until the equilibrium Fermi levels are reached on both sides. The DFT calculation was carried out using the periodic plate model of ZnNiCo LDH (010)/MXene (002) (Fig. 4(e)), as shown in the atomic model. Among them, nickel (silver), cobalt (dark blue), zinc (dark gray), carbon (dark brown), titanium (light blue), hydrogen (pink), and oxygen (red) atoms are color-coded in a stoichiometric ratio of Ni:Co:Zn of 3:2:1, and the cross-sectional and top view charge density diagrams (Fig. 4(f)) show obvious interfacial charge redistribution. On the LDH (blue) side, electron-rich regions form, and electron-deficient regions appear on the MXene (yellow) side, due to the spontaneous transfer of electrons from the N-type semiconductor LDH to the metallic MXene [57, 58], which indicates that the BIEF heterointerface contributes to enhancing the electrical conductivity of ZNCM. In this case, BIEF can be established in the space charge separation region extending from LDH to MXene [59].

For a more intuitive comparison of electromagnetic wave absorption performance across different specimens, reflection loss (RL) was calculated using transmission line theory and a typical metal support model. Calculating RL allows for a visual evaluation of electromagnetic wave absorption capacity. The formula is as shown in Eq. (4) [26]

$$RL = 20\lg\left|\frac{Z_{in} - Z_0}{|Z_{in} + Z_0|}\right| \quad (4)$$

where Z_{in} and Z_0 represent the input impedance and free space impedance (377 Ω) of the absorber respectively. Z_{in} is calculated by Eq. (5) [60, 61]

$$Z_{in} = Z_0\sqrt{\frac{\mu_r}{\varepsilon_r}}\tanh\left(j\frac{2\pi f d}{c}\sqrt{2\mu_r\varepsilon_r}\right) \quad (5)$$

where f is the frequency of the electromagnetic wave, d is the thickness of the wave absorbing material, and c is the speed of light. Figure 5 shows the influence of different material thicknesses on the absorption strength. Appropriate material thickness significantly enhances absorption strength. Materials with optimal thickness achieve superior microwave absorption at reduced thickness, while thinner matching thicknesses deviate from practical feasibility. Figures 5(a) and 5(f), and Fig. S8(k) in the ESM show the minimum RL (RL_{min}) of pure LDH at a thickness of 3.5 mm is −3.58 dB, and the maximum effective absorption bandwidth (EAB) is 0. Pure MXene mainly relies on dielectric loss to consume EMW, and its EMW absorption performance is poor. When the thickness is 1.5 mm, the RL_{min} is −7.95 dB, as shown in Figs. 5(b) and 5(g), and Fig. S8(l) in the ESM, and the maximum EAB is also 0. After integrating LDH and MXene to form ZNCM composites, the absorption performance of EMW was significantly improved. The RL_{min} and EAB of ZNCM-10 (Figs. 5(c) and 5(h), and Fig. S8(m) in the ESM) reached −47.8 dB at thicknesses of 1.45 mm and 3.41 GHz, respectively. Compared with ZNCM-10, the RL_{min} and EAB of ZNCM-20 are slightly decreased, which may be due to the imbalance between impedance matching and attenuation capacity. The RL_{min} of ZNCM-20 (Figs. 5(d) and 5(i), and Fig. S8(n) in the ESM) at a thickness of 1.99 mm was −40.81 dB. Meanwhile, the EAB of ZNCM-20 decreased to 3.26 GHz. It is worth noting that the RL_{min} of ZNCM-30 (Figs. 5(e) and 5(j), and Fig. S8(o) in the ESM) at a thickness of 2.2 mm is −49.39 dB and the wide EAB is 3.08 GHz, which is crucial for the development of a new generation of EMW absorbing materials. By changing the matching thickness, the EAB of ZNCM-30 can cover a considerable part of the measured frequency. The influence of different packing loads on the electromagnetic wave loss capacity has also been studied. With an increase in ZNCM loading from 20 wt.% to 30 wt.%, the frequency of RL_{min} shifted toward lower frequencies (Figs. S9–S11 in the ESM). In conclusion, by changing the composite amount of $Ti_3C_2T_x$ nanosheets, the electromagnetic parameters and microwave absorption capacity of ZNCM composites can be slightly adjusted. Such flexibility offers a degree of adaptability for optimizing the absorption performance of composite materials with varying application requirements.

The quantitative analysis of three-dimensional (Figs. 5(k) and 5(n)) and two-dimensional histograms (Figs. 5(i) and 5(o), and Table S4 in the ESM) systematically demonstrated the superior EMW absorption capability of ZNCM, achieving an outstanding RL_{min} (RL_{min} = −49.8 dB) at an ultra-low thickness (1.45 mm). Effective absorption bandwidth is wide (EAB = 3.4 GHz, covering 12.4–18.7 GHz). Comparison with state-of-the-art absorbents (Figs. 5(m) and 5(p), Table S5 in the ESM) reveals that ZNCM surpasses the latest benchmark material by 42% in RL_{min} and 28% in EAB, directly attributed to its bioinspired coral reef structure. Hierarchical design collaboratively optimizes interface polarization through micro-capacitive LDH/MXene

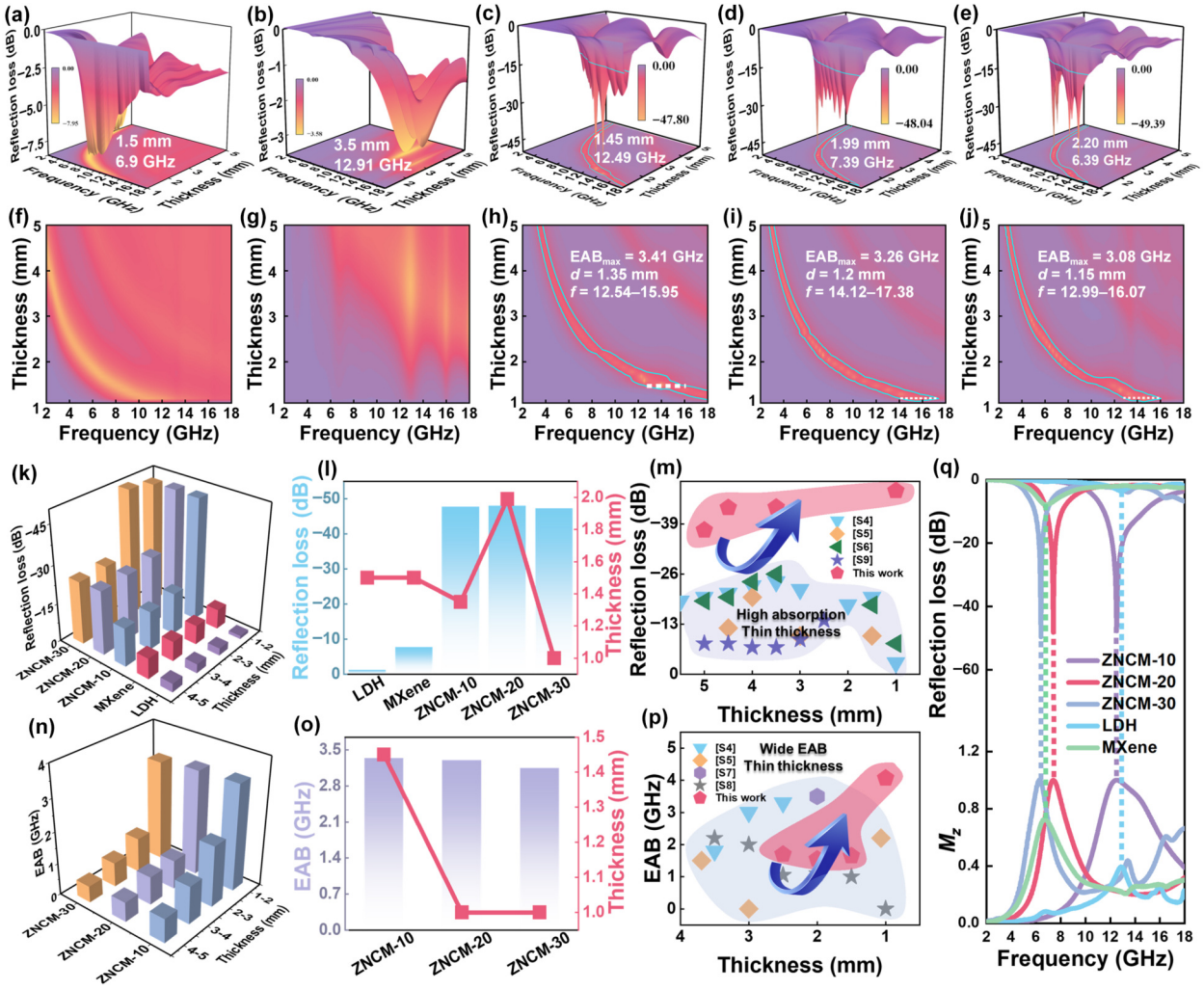

Figure 5 Three-dimensional reflection loss diagrams of (a) MXene, (b) ZnNiCo LDH, (c) ZNCM-10, (d) ZNCM-20, and (e) ZNCM-30 within the range of 2–18 GHz, and (f)–(j) corresponding two-dimensional projection diagrams. (k) The comparison bar charts of reflection loss of samples at different thicknesses, (l) two-dimensional comparison bar charts, and (m) comparison charts of working thickness-reflection loss with the remaining MXene bases. (n)–(p) Comparison bar charts of the maximum absorption loan of the samples at different thicknesses, two-dimensional comparison bar charts, and comparison charts with the working thickness maximum absorption bandwidth of the remaining MXene bases. (q) The reflection loss of the sample is matched with the impedance.

heterojunctions, and simultaneously enhances multiple scattering through interpenetrating porous networks.

To validate the efficacy of our coral reef-inspired cavity structure in regulating the impedance matching of high-conductivity MXene-based composites, impedance matching analysis was conducted on the samples (Fig. 5(q)). The primary consideration is impedance matching coefcient (M_z). For samples with fnite thickness, utilizing M_z to evaluate impedance matching characteristics is more reasonable, and value near 1.0 indicates a well-matched impedance, with a large number of EM waves able to be introduced into materials. An assessment of the impedance matching capability of absorbers is conducted within the range of 0.8 to 1.0. The value of M_z were determined by the subsequent equation [62, 63]

$$M_z = \frac{2Z'_{in}}{|Z_{in}|^2 + 1} \quad (6)$$

The impedance matching coefficient of LDH is significantly below 1 (0.394), attributable to its poor electrical conductivity that fails to induce electromagnetic wave dissipation. Conversely, pure MXene exhibits a suboptimal impedance matching coefficient (0.722), which stems from the skin effect induced by its high conductivity. In the ZNCM composite, however, precise tuning of the LDH to MXene ratio (from 3:1 to 1:1) achieves near-ideal impedance characteristics ($M_z \approx 1$) across the 2–18 GHz. As the $Ti_3C_2T_x$ MXene content increases, the peak of the characteristic impedance shifts toward lower frequencies. This frequency shift correlates with the trend of RL_{min}, indicating that the absorption frequency range of the composite can be tailored by adjusting the MXene content. We propose that the regulation of impedance matching in this sample is primarily mediated by the synergistic loss mechanism at the heterojunction interface of the hierarchical porous structure. Specifically, the electronegativity difference between LDH and MXene induces pronounced interfacial polarization, while the MXene conductive network facilitates conduction loss via electron hopping. These effects, in tandem with the scattering effect of the coral reef-like porous structure, achieve a balance between dielectric loss and impedance matching.

RCS serves as a pivotal metric for evaluating far-field microwave absorption performance (Fig. 6(a)). The model employed plane wave excitation along the $-Z$ axis with θ as the detection angle,

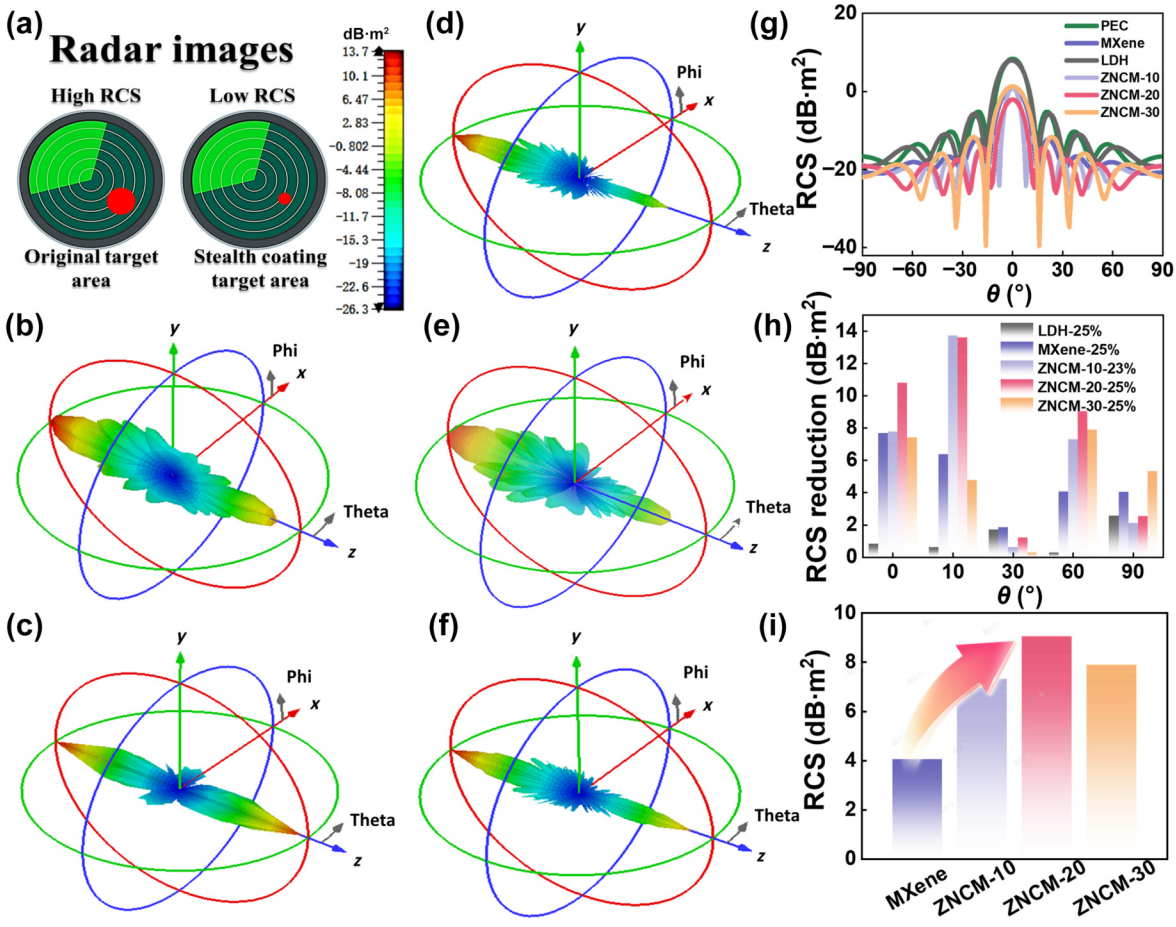

Figure 6 (a) Schematic diagram of the principle of the radar scattering cross-section. (b)–(f) Three-dimensional RCS images of PEC substrates with MXene, ZnNiCo LDH, ZNCM-10, ZNCM-20, and ZNCM-30. (g) 1D RCS plots with angles ranging from −90° to +90°. (g) Two-dimensional graph of radar cross-section. (h) The reduction of RCS is achieved by subtracting the composite material from PEC. (i) Compared with LDH, the RCS reduction values of MXene, ZNCM-10, ZNCM-20, and ZNCM-30.

testing LDH, MXene, ZNCM-10, ZNCM-20, and ZNCM-30 coatings, the electromagnetic wave absorption ability is shown in Table S6 in the ESM. Three-dimensional RCS patterns at 16 GHz (Figs. 6(b)–6(f)) demonstrate reflection intensity variations across materials. ZNCM-coated substrates exhibit significantly reduced backscattering, confirming enhanced EMW attenuation through bioinspired coral-like structures. Quantitative 2D angular analysis (Fig. 6(g)) reveals ZNCM-30 achieves the lowest RCS (−39.57 dB·m²), outperforming bare PEC by a wide margin. Further analysis of intrinsic absorption capabilities (Fig. 6(h)) shows ZNCM-10 delivers a maximum RCS reduction of 13.74 dB·m² at θ = 10°, surpassing LDH and MXene. Angle-specific comparisons (Fig. 6(i)) highlight ZNCM-20 9.05 dB·m² RCS reduction over LDH at θ = 10°, directly linked to its optimized impedance matching. Critically, the coral-like hierarchical architecture synergistically enhances EMW dissipation through: Multi-reflection trapping within interconnected pores. Interfacial polarization at LDH/MXene junctions. This dual mechanism enables broadband RCS suppression across military relevant frequencies, validating ZNCM composites as effective stealth coating materials.

MA mechanism of unique three-dimensional layered ZNCM composite is illustrated in Fig. 7. Hollow layered structures with open voids enhance impedance matching, reduce absorber weight, and boost interfacial polarity. Curved $Ti_3C_2T_x$ MXene sheets, randomly oriented, establish a three-dimensional conductive network. Electrons move freely along conductive paths, transforming electromagnetic wave energy into thermal energy. Such electron migration strengthens conduction loss and aids in electromagnetic wave dissipation. Achieving multiple reflections and scattering through 3D porous layered ZNCM composites extends the electromagnetic wave transmission path. Extended paths heighten wave material interaction time, thereby enhancing energy conversion and dissipation. Terminal functional groups and inherent defects in layered $Ti_3C_2T_x$ MXene, coupled with oxygen vacancies in ZNCM due to activation, synergistically optimize impedance matching. Simultaneously, they elevate dipole and defect polarization. High-density heterogeneous interfaces are provided by the 3D layered structures formed via $Ti_3C_2T_x$ MXene sheets and ZnNiCo LDH. These interfaces result in space charge accumulation and uneven distribution, generating macroscopic electrical moments. Consequently, observable interfacial polarization, termed the Maxwell–Wagner effect, emerges.

4 Conclusion

This work represents the first integration of a trimetallic LDH/MXene heterostructure into a coral-inspired architecture, resolving the impedance matching dilemma of MXene absorbers through multi-interface engineering of built-in electric fields. The

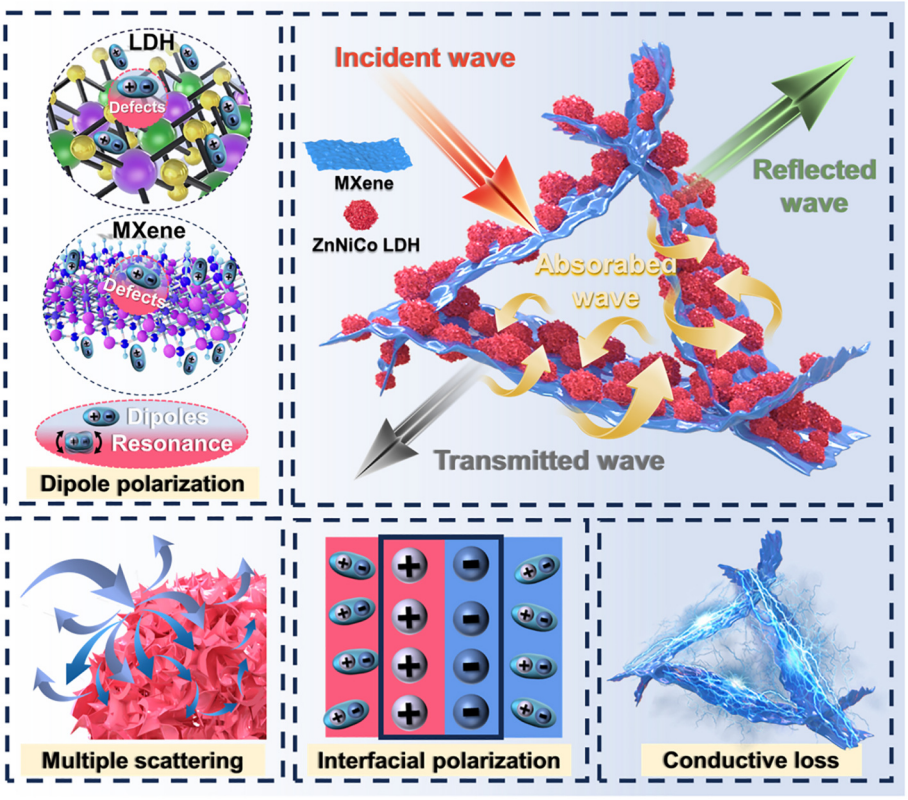

Figure 7 Electromagnetic wave absorption mechanism of ZNCM samples.

design constructs continuous networks of Mott–Schottky interfaces via electrostatic assembly of polar semiconductor units and conductive matrices. Vertical growth of flower-like LDH on MXene establishes multi-level propagation paths of electromagnetic waves. This configuration generates high-density built-in electric fields across the heterostructure. Key innovations include the first integration of coral-like structures into MXene absorbers for resolving impedance matching dilemmas and the creation of seamless BIEF networks through controlled formation of semiconductor-conductor interfaces. Synergistic enhancement of interfacial polarization and conductive loss mechanisms occurs. Exceptional performance confirms the approach with remarkable −49.6 dB reflection loss at ultralow thickness of 1.35 mm. Effective absorption bandwidth reaches 3.4 GHz across Ku-band frequencies. Significant reduction of radar cross-section is validated at −39.57 dB·m^2. These achievements fulfill the paradigm of thin, light, wide, and strong absorption. The work provides fundamental insights into manipulation of built-in electric fields through multi-interface engineering. It establishes a new biomimetic strategy for advanced electromagnetic wave absorption materials. This research opens avenues for next-generation stealth technologies and electromagnetic protection systems.

Electronic Supplementary Material: Supplementary material (comprehensive data on ZnNiCo LDH/$Ti_3C_2T_x$ MXene (ZNCM) composites for microwave absorption, including ZNCM component ratios and PVDF filling ratios, material characterization data (XRD, XPS, SEM/TEM for morphology, elemental content, and zeta potential), electromagnetic parameters , and microwave absorption performance data; RCS simulation data of samples at 0°–180° incident angles and comparative data of ZNCM composites with other MXene-based microwave absorbers, and all serving to validate the enhanced microwave absorption performance of bionic coral reef-inspired ZNCM composites) is available in the online version of this article at https://doi.org/10.26599/NR.2025.94907842.

Data availability

All data needed to support the conclusions in the paper are presented in the manuscript and the Electronic Supplementary Material. Additional data related to this paper may be requested from the corresponding author upon request.

Acknowledgements

This work was supported by the Fundamental Research Funds for the Central Universities (No. 2025YJS170) and the National Natural Science Foundation of China (No. 52172081). The authors would like to thank Shiyanjia Lab (www. shiyanjia. com) for the XPS characterizations.

Declaration of competing interest

All the contributing authors declare no interest conflict. They have no known competing financial interests or personal relationships that could have appeared to influence the work reported in this paper.

Author contribution statement

Y. T. M.: Writing – review & editing, writing – original draft, methodology, investigation, conceptualization. B. C.: Methodology,

investigation, formal analysis, conceptualization. L. Z.: Methodology, investigation, formal analysis, conceptualization. Y. Z.: Methodology, investigation, formal analysis, conceptualization. Y. T. Z.: Writing – review & editing, data curation. J. H. W.: Writing – review & editing, data curation. G. S.: Writing – review & editing, data curation. L. T. Y.: Writing – review & editing, project administration, funding acquisition, formal analysis, conceptualization. M. L.: Writing – review & editing, project administration. B. L. L.: Writing – review & editing, project administration, funding acquisition, formal analysis, conceptualization. G. S. W.: Writing – review & editing, project administration. All the authors have approved the final manuscript.

Use of AI statement

During the preparation of this work, the authors used deepseek in order to spelling and grammar checks. After using this tool, the authors reviewed and edited the content as needed and take full responsibility for the content ofhe publication.

References

[1] Fan, X. X.; Zhang, X. C.; Li, L.; Cao, M. S. Recent progress and perspective of microwave absorption materials derived from metal-organic frameworks. *Soft Sci.* **2024**, *4*, 43.

[2] Zhao, Z. H.; Qing, Y. C.; Kong, L.; Xu, H. L.; Fan, X. M.; Yun, J. J.; Zhang, L. M.; Wu, H. J. Advancements in microwave absorption motivated by interdisciplinary research. *Adv. Mater.* **2024**, *36*, 2304182.

[3] Yele, M.; Sarula, G.; Yang, J.; Yang, L.; Zhang, H.; Chen, L. F.; Zhang, X. M.; Wang, J. H.; Wang, T. Y.; Jin, C. Z. et al. Integrated structural-functional MXene-GNs/ANF flexible composite film with enhanced thermal conductivity and electromagnetic interference shielding performance. *J. Mater. Sci. Technol.* **2026**, *241*, 200–210.

[4] Liu, S.; Zhou, D. F.; Huang, F.; He, M.; Qin, S. H.; Shi, Y. Q.; Song, P. A. Heterointerface engineering of polymer-based electromagnetic wave absorbing materials. *Soft Sci.* **2025**, *5*, 7.

[5] Cai, B.; Zhou, L.; Zhao, P. Y.; Peng, H. L.; Hou, Z. L.; Hu, P. F.; Liu, L. M.; Wang, G. S. Interface-induced dual-pinning mechanism enhances low-frequency electromagnetic wave loss. *Nat. Commun.* **2024**, *15*, 3299.

[6] Han, Y. X.; Ruan, K. P.; Gu, J. W. Multifunctional thermally conductive composite films based on fungal tree-like heterostructured silver nanowires@boron nitride nanosheets and aramid nanofibers. *Angew. Chem., Int. Ed.* **2023**, *62*, e202216093.

[7] He, P.; Cao, M. S.; Cao, W. Q.; Yuan, J. Developing MXenes from wireless communication to electromagnetic attenuation. *Nano-Micro Lett.* **2021**, *13*, 115.

[8] Liu, A.; Qiu, H.; Lu, X. H.; Guo, H.; Hu, J. W.; Liang, C. B.; He, M. K.; Yu, Z.; Zhang, Y. L.; Kong, J. et al. Asymmetric structural MXene/PBO aerogels for high-performance electromagnetic interference shielding with ultra-low reflection. *Adv. Mater.* **2025**, *37*, 2414085.

[9] Ming, W.; Yang, L.; Chen, H. X.; Fei, F.; Zhang, H.; Sarula, G.; Wang, J. H.; Wang, T. Y.; Jin, C. Z.; Liang, B. L. et al. High toughness MXene/ANF-CZIF67/ANF "magnetic-electric" Janus film for multifunctional low reflection electromagnetic interference shielding. *Nano Res.*, in press, DOI: 10.26599/NR.2025.94907621.

[10] Cao, M. S.; Song, W. L.; Hou, Z. L.; Wen, B.; Yuan, J. The effects of temperature and frequency on the dielectric properties, electromagnetic interference shielding and microwave-absorption of short carbon fiber/silica composites. *Carbon* **2010**, *48*, 788–796.

[11] Li, W.; Liu, J. W.; Liang, B. L.; Shu, Y. Q.; Wang, J. F. Small molecule hydrogen-bonded toughen nacre-inspired montmorillonite-konjac glucomannan-glycerin film with superior mechanical, transparent and UV-blocking properties. *Compos. Part B: Eng.* **2021**, *204*, 108492.

[12] Wang, H. Y.; Sun, X. B.; Yang, S. H.; Zhao, P. Y.; Zhang, X. J.; Wang, G. S.; Huang, Y. 3D Ultralight hollow NiCo compound@MXene composites for tunable and high-efficient microwave absorption. *Nano-Micro Lett.* **2021**, *13*, 206.

[13] Gao, X. R.; Jia, Z. R.; Wang, B. B.; Wu, X. M.; Sun, T.; Liu, X. H.; Chi, Q. G.; Wu, G. L. Synthesis of NiCo-LDH/MXene hybrids with abundant heterojunction surfaces as a lightweight electromagnetic wave absorber. *Chem. Eng. J.* **2021**, *419*, 130019.

[14] Zhang, X.; Qiao, J.; Jiang, Y. Y.; Wang, F. L.; Tian, X. L.; Wang, Z.; Wu, L. L.; Liu, W.; Liu, J. R. Carbon-based MOF derivatives: Emerging efficient electromagnetic wave absorption agents. *Nano-Micro Lett.* **2021**, *13*, 135.

[15] Zhang, Z. W.; Cai, Z. H.; Wang, Z. Y.; Peng, Y. L.; Xia, L.; Ma, S. P.; Yin, Z. Z.; Huang, Y. A review on metal-organic framework-derived porous carbon-based novel microwave absorption materials. *Nano-Micro Lett.* **2021**, *13*, 56.

[16] Zhong, X.; He, M. K.; Zhang, C. Y.; Guo, Y. Q.; Hu, J. W.; Gu, J. W. Heterostructured BN@Co–C@C endowing polyester composites excellent thermal conductivity and microwave absorption at C band. *Adv. Funct. Mater.* **2024**, *34*, 2313544.

[17] Zhan, B. B.; Hao, Y. L.; Qi, X. S.; Qu, Y. P.; Ding, J. F.; Yang, J. L.; Gong, X.; Chen, Y. L.; Peng, Q.; Zhong, W. Multifunctional cellular carbon foams derived from chitosan toward self-cleaning, thermal insulation, and highly efficient microwave absorption properties. *Nano Res.* **2024**, *17*, 927–938.

[18] He, M. K.; Hu, J. W.; Yan, H.; Zhong, X.; Zhang, Y. L.; Liu, P. B.; Kong, J.; Gu, J. W. Shape anisotropic chain-like CoNi/polydimethylsiloxane composite films with excellent low-frequency microwave absorption and high thermal conductivity. *Adv. Funct. Mater.* **2025**, *35*, 2316691.

[19] Zhang, K. L.; Liu, Y. H.; Liu, Y. A.; Yan, Y. F.; Ma, G. S.; Zhong, B.; Che, R. C.; Huang, X. X. Tracking regulatory mechanism of trace Fe on graphene electromagnetic wave absorption. *Nano-Micro Lett.* **2024**, *16*, 66.

[20] Yan, H.; Xuan, S. Y.; Fan, X.; Shan, Y. M.; Xu, X. Y.; Yao, X. F. A repair efficiency evaluation framework for the honeycomb microwave absorbing structure. *Compos. Sci. Technol.* **2024**, *248*, 110471.

[21] Wang, H. Y.; Hu, P. F.; Sun, X. B.; Hou, Z. L.; Zhao, P. Y.; Zhou, L.; Yang, S. H.; Geng, C. Y.; Zhu, Y. F.; Wu, X. J. et al. Bioinspired disordered aerogel for omnidirectional terahertz response. *Adv. Mater.* **2025**, *37*, 2418889.

[22] Zhan, B. B.; Qu, Y. P.; Qi, X. S.; Ding, J. F.; Shao, J. J.; Gong, X.; Yang, J. L.; Chen, Y. L.; Peng, Q.; Zhong, W. et al. Mixed-dimensional assembly strategy to construct reduced graphene oxide/carbon foams heterostructures for microwave absorption, anti-corrosion and thermal insulation. *Nano-Micro Lett.* **2024**, *16*, 221.

[23] Zhang, K. L.; Yan, Y. F.; Wang, Z.; Ma, G. S.; Jia, D. C.; Huang, X. X.; Zhou, Y. Integration of electrical properties and polarization loss modulation on atomic Fe–N-RGO for boosting electromagnetic wave absorption. *Nano-Micro Lett.* **2025**, *17*, 46.

[24] Liang, Q. Q.; He, M. K.; Zhan, B. B.; Guo, H.; Qi, X. S.; Qu, Y. P.; Zhang, Y. L.; Zhong, W.; Gu, J. W. Yolk-shell CoNi@N-doped carbon-CoNi@CNTs for enhanced microwave absorption, photothermal, anti-corrosion, and antimicrobial properties. *Nano-Micro Lett.* **2025**, *17*, 167.

[25] Wangpraseurt, D.; You, S. T.; Azam, F.; Jacucci, G.; Gaidarenko, O.; Hildebrand, M.; Kühl, M.; Smith, A. G.; Davey, M. P.; Smith, A. et al. Bionic 3D printed corals. *Nat. Commun.* **2020**, *11*, 1748.

[26] Ma, Z. L.; Kang, S. L.; Ma, J. Z.; Shao, L.; Zhang, Y. L.; Liu, C.; Wei, A. J.; Xiang, X. L.; Wei, L. F.; Gu, J. W. Ultraflexible and mechanically strong double-layered aramid nanofiber-$Ti_3C_2T_x$ MXene/silver nanowire nanocomposite papers for high-performance electromagnetic interference shielding. *ACS Nano* **2020**, *14*, 8368–8382.

[27] Han, X. P.; Ling, X. F.; Wang, Y.; Ma, T. Y.; Zhong, C.; Hu, W. B.; Deng, Y. D. Generation of nanoparticle, atomic-cluster, and single-atom cobalt catalysts from zeolitic imidazole frameworks by spatial isolation and their use in zinc-air batteries. *Angew. Chem., Int. Ed.* **2019**, *58*, 5359–5364.

[28] Meng, Y. T.; Liang, C. M.; Jiang, D.; Zhang, Y.; Su, J. H.; Xu, X. H.; Lu, M. ZnNiCo layered double hydroxide@MXene with 2D/2D hierarchical structure derived from micro-sized ZIF-8/67 anchored to Mxene for asymmetric supercapacitors. *Chem. Eng. J.* **2024**, *479*, 147695.

[29] Zhang, Y. H.; Zhang, L.; Si, H. X.; Zhang, Y.; Li, C. P.; Zhang, L.; Zhang, J. W.; Gong, C. H. TiN nanofiber metacomposites for efficient electromagnetic wave absorption: Insights on multiple reflections and scattering effects. *J. Mater. Sci. Technol.* **2025**, *233*, 69–79.

[30] Wang, J. E.; Song, T. L.; Ming, W.; Yele, M.; Chen, L. F.; Zhang, H.; Zhang, X. J.; Liang, B. L.; Wang, G. S. High MXene loading, nacre-inspired MXene/ANF electromagnetic interference shielding composite films with ultralong strain-to-failure and excellent Joule heating performance. *Nano Res.* **2024**, *17*, 2061–2069.

[31] Han, Y. X.; Ruan, K. P.; He, X. Y.; Tang, Y. S.; Guo, H.; Guo, Y. Q.; Qiu, H.; Gu, J. W. Highly thermally conductive aramid nanofiber composite films with synchronous visible/infrared camouflages and information encryption. *Angew. Chem., Int. Ed.* **2024**, *63*, e202401538.

[32] Chen, X.; Wang, K. Y.; Xie, K.; Tao, H. J.; Wang, Y. Q. MXene-coated nickel ion-exchanged ZIF skeleton-cavity layered double hydroxides for supercapacitors. *Energy Fuels* **2023**, *37*, 763–773.

[33] Gao, Y.; Lin, J. J.; Chen, X.; Tang, Z. D.; Qin, G.; Wang, G. Engineering 2D MXene and LDH into 3D hollow framework for boosting photothermal energy storage and microwave absorption. *Small* **2023**, *19*, 2303113.

[34] Wu, Z. M.; Huang, J.; Zeng, X. J. Dual magnetic particles modified carbon nanosheets in CoFe/Co@NC heterostructure for efficient electromagnetic synergy. *Soft Sci.* **2024**, *4*, 42.

[35] Liang, W. H.; Wu, J. T.; Zhang, S.; Zhao, P. Y.; Cong, Y.; Guo, Y. Q.; Wang, G. S. Porous $Ti_3C_2T_x$ MXene nanosheets sandwiched between polyimide fiber mats for electromagnetic interference shielding. *Nano Res.* **2024**, *17*, 2070–2078.

[36] Liu, T. T.; Zheng, Q.; Cao, W. Q.; Wang, Y. Z.; Zhang, M.; Zhao, Q. L.; Cao, M. S. *In situ* atomic reconstruction engineering modulating graphene-like MXene-based multifunctional electromagnetic devices covering multi-spectrum. *Nano-Micro Lett.* **2024**, *16*, 173.

[37] Wang, J. E.; Ming, W.; Chen, L. F.; Song, T. L.; Yele, M.; Zhang, H.; Yang, L.; Sarula, G.; Liang, B. L.; Yan, L. T. et al. MoS_2 lubricate-toughened MXene/ANF composites for multifunctional electromagnetic interference shielding. *Nano-Micro Lett.* **2025**, *17*, 36.

[38] Yuan, M. Y.; Zhao, B.; Yang, C. D.; Pei, K.; Wang, L. Y.; Zhang, R. X.; You, W. B.; Liu, X. H.; Zhang, X. F.; Che, R. C. Remarkable magnetic exchange coupling via constructing bi-magnetic interface for broadband lower-frequency microwave absorption. *Adv. Funct. Mater.* **2022**, *32*, 2203161.

[39] Liang, C. B.; Qiu, H.; Song, P.; Shi, X. T.; Kong, J.; Gu, J. W. Ultra-light MXene aerogel/wood-derived porous carbon composites with wall-like "mortar/brick" structures for electromagnetic interference shielding. *Sci. Bull.* **2020**, *65*, 616–622.

[40] Peng, H. L.; Cai, B.; Zhang, Y.; Gao, L. C.; Zhao, P. Y.; Zhou, L.; Zhang, S.; Liang, W. H.; Xuan, Q. F.; Koo, M. C. et al. Radar-terahertz-infrared compatible stealth coaxial silver nanowire@carbon nano-cable aerogel. *Angew. Chem., Int. Ed.* **2025**, *64*, e202421090.

[41] Qin, G.; Qiu, J. Graphene/polypyrrole nanocomposites with high negative permittivity and low dielectric loss tangent. *Ceram. Int.* **2019**, *45*, 5407–5412.

[42] Ko, Y.; Yoon, H.; Kwon, S.; Lee, H.; Park, M.; Jeon, I.; Lim, J. A.; Chung, S.; Lee, S. S.; Sung, B. J. et al. Elastomeric high-κ composites of low dielectric loss tangent: Experiment and simulation. *Compos. Part B: Eng.* **2020**, *201*, 108337.

[43] Lv, H. L.; Yang, Z. H.; Wang, P. L.; Ji, G. B.; Song, J. Z.; Zheng, L. R.; Zeng, H. B.; Xu, Z. J. A voltage-boosting strategy enabling a low-frequency, flexible electromagnetic wave absorption device. *Adv. Mater.* **2018**, *30*, 1706343.

[44] Zhang, Y.; Si, H. X.; Dai, Z. Y.; Zhang, W.; Hao, B.; Li, C. P.; Zhang, J. W.; Gong, C. H. Subwavelength-scale graphene aerogel powders for efficient microwave absorption composites with improved mechanical strength. *Chem. Eng. J.* **2025**, *505*, 159118.

[45] Liu, M.; Chen, G. Y.; Liang, G. S.; Qian, Y. T.; Yang, L. T.; Che, R. C. Asymmetric atomic diffusion-engineered magnetic nano-interfaces for enhanced low-frequency electromagnetic wave attenuation. *Adv. Funct. Mater.*, in press, DOI: 10.1002/adfm.202508174.

[46] Zhang, Y. L.; Ruan, K. P.; Zhou, K.; Gu, J. W. Controlled distributed $Ti_3C_2T_x$ hollow microspheres on thermally conductive polyimide composite films for excellent electromagnetic interference shielding. *Adv. Mater.* **2023**, *35*, 2211642.

[47] Li, H. Y.; Bowen, C. R.; Dan, H. Y.; Yang, Y. Pyroelectricity induced by Schottky interface above the Curie temperature of bulk materials. *Joule* **2024**, *8*, 401–415.

[48] Cheng, J. Y.; Zhang, H. B.; Ning, M. Q.; Raza, H.; Zhang, D. Q.; Zheng, G. P.; Zheng, Q. B.; Che, R. C. Emerging materials and designs for low- and multi-band electromagnetic wave absorbers: The search for dielectric and magnetic synergy. *Adv. Funct. Mater.* **2022**, *32*, 2200123.

[49] He, M. K.; Zhong, X.; Lu, X. H.; Hu, J. W.; Ruan, K. P.; Guo, H.; Zhang, Y. L.; Guo, Y. Q.; Gu, J. W. Excellent low-frequency microwave absorption and high thermal conductivity in polydimethylsiloxane composites endowed by hydrangea-like CoNi@BN heterostructure fillers. *Adv. Mater.* **2024**, *36*, 2410186.

[50] Zhou, J.; Guo, H.; Di, J.; Liu, G. G.; Jiang, W. Multistage coupling of interface and core–shell engineering of a cobalt-based heterostructure for integration of multiple electromagnetic absorption. *J. Mater. Chem. A* **2023**, *11*, 20055–20064.

[51] Che, R. C.; Gu, J. W.; Kong, J.; Lu, W.; Huang, Y.; Lv, H. L.; Liu, X. F.; Qi, X. S.; Wu, G. L.; Wu, H. J. Designing future nanomaterials for electromagnetic wave absorption and shielding. *Cell Rep. Phys. Sci.* **2025**, *6*, 102502.

[52] Ma, Z. L.; Xiang, X. L.; Shao, L.; Zhang, Y. L.; Gu, J. W. Multifunctional wearable silver nanowire decorated leather nanocomposites for joule heating, electromagnetic interference shielding and piezoresistive sensing. *Angew. Chem., Int. Ed.* **2022**, *61*, e202200705.

[53] Dai, B.; Ma, Y.; Dong, F.; Yu, J.; Ma, M. L.; Thabet, H. K.; El-Bahy, S. M.; Ibrahim, M. M.; Huang, M. N.; Seok, I. et al. Overview of MXene and conducting polymer matrix composites for electromagnetic wave absorption. *Adv. Compos. Hybrid Mater.* **2022**, *5*, 704–754.

[54] Wang, L.; Lu, J. T.; Zhang, J. L.; Zhu, J. F. Facile preparation and high microwave absorption of flower-like carbon nanosheet aggregations embedded with ultrafine Mo_2C. *J. Colloid Interface Sci.* **2023**, *641*, 729–736.

[55] Lv, H. L.; Yao, Y. X.; Yuan, M. Y.; Chen, G. Y.; Wang, Y. C.; Rao, L. J.; Li, S. C.; Kara, U. I.; Dupont, R. L.; Zhang, C. et al. Functional nanoporous graphene superlattice. *Nat. Commun.* **2024**, *15*, 1295.

[56] Xiao, J. X.; Zhan, B. B.; He, M. K.; Qi, X. S.; Gong, X.; Yang, J. L.; Qu, Y. P.; Ding, J. F.; Zhong, W.; Gu, J. W. Interfacial polarization loss improvement induced by the hollow engineering of necklace-like PAN/carbon nanofibers for boosted microwave absorption. *Adv. Funct. Mater.* **2025**, *35*, 2316722.

[57] Wang, J. K.; Li, X. N.; Liang, H. J.; Zhang, C. X.; Du, H. Y.; Sun, Y.; Li, H.; Pan, H. G.; Hao, Y. Y.; Zhao, M. et al. Built-in electric field in 2D/2D LDH/antimonene heterostructure to induce stable β-NiOOH at ultralow potential for cost-effective water electrolysis. *Adv. Funct. Mater*., in press, DOI: 10.1002/adfm.202503596.

[58] Song, P.; Liu, B.; Liang, C. B.; Ruan, K. P.; Qiu, H.; Ma, Z. L.; Guo, Y. Q.; Gu, J. W. Lightweight, flexible cellulose-derived carbon aerogel@reduced graphene oxide/PDMS composites with outstanding EMI shielding performances and excellent thermal conductivities. *Nano-Micro Lett.* **2021**, *13*, 91.

[59] Gao, Z. G.; Iqbal, A.; Hassan, T.; Hui, S. C.; Wu, H. J.; Koo, C. M. Tailoring built-in electric field in a self-assembled zeolitic imidazolate framework/MXene nanocomposites for microwave absorption. *Adv. Mater.* **2024**, *36*, 2311411.

[60] Han, Y. X.; Guo, H.; Qiu, H.; Hu, J. W.; He, M. K.; Shi, X. T.; Zhang, Y. L.; Kong, J.; Gu, J. W. Multimechanism decoupling for low-frequency microwave absorption hierarchical Fe-doped Co magnetic microchains. *Adv. Funct. Mater*., in press, DOI: 10.1002/adfm.202506803.

[61] Cao, X. H.; Wu, X. Y.; Wang, X.; Luo, J. M.; Zhang, Z.; Xue, Y.; Zhang, G. L.; Zhang, L. Y.; Zhang, H.; Yu, J. Y. Mechanistic insights into the structural evolution of ZIF-67 via electrospinning strategy toward high electromagnetic wave absorption performance of ZIF-67-derived carbon nanofibers. *Adv. Sci.* **2025**, *12*, 2502560.

[62] Zhang, Y.; Hu, P. F.; Zhao, P. Y.; Cai, B.; Peng, H. L.; Yang, S. H.; Koo, M. C.; Liang, C. M.; Wang, G. S. Phosphorus vacancy-induced built-in electric field for electromagnetic properties modulation. *Adv. Sci*., in press, DOI: 10.1002/advs.202502857.

[63] Zhang, Y.; Yang, S. H.; Xin, Y.; Cai, B.; Hu, P. F.; Dai, H. Y.; Liang, C. M.; Meng, Y. T.; Su, J. H.; Zhang, X. J. et al. Designing symmetric gradient honeycomb structures with carbon-coated iron-based composites for high-efficiency microwave absorption. *Nano-Micro Lett.* **2024**, *16*, 234.